Journal of Alloys and Compounds 726 (2017) 352–357

Contents lists available at ScienceDirect

Journal of Alloys and Compounds

journal homepage: http://www.elsevier.com/locate/jalcom

Correlation between local structure and magnetic behavior in co-sputtered $Tb_xFe_{73}Ga_{27-x}$ ($7 \leq x \leq 11$) thin films

A. Muñoz-Noval [a], E. Salas-Colera [b], P. Bartolomé [c], A. Serrano [b], G.R. Castro [b], R. Ranchal [c, *]

[a] Department of Applied Chemistry, Hiroshima University, Higashi-hiroshima, 739-8527, Hiroshima, Japan
[b] BM25-Spline, the Spanish CRG at the ESRF, Grenoble, France and Instituto de Ciencia de Materiales de Madrid-CSIC, Madrid, Spain
[c] Dpto. Física de Materiales, Facultad de Ciencias Físicas, Universidad Complutense de Madrid, Ciudad Universitaria s/n, Madrid 28040, Spain

ARTICLE INFO

Article history:
Received 18 May 2017
Received in revised form
6 July 2017
Accepted 26 July 2017
Available online 29 July 2017

Keywords:
Sputtering
Iron alloys
X-ray absorption fine structure
Magnetic properties

ABSTRACT

We report on the evolution of the microstructure of Tb-Fe-Ga films deposited by co-sputtering from $Tb_{33}Fe_{67}$ and $Fe_{72}Ga_{28}$ targets. The sputtering power was fixed (90 W) in the $Fe_{72}Ga_{28}$ whereas it was increased from 50 to 90 W in the $Tb_{33}Fe_{67}$ target resulting on $Tb_xFe_{73}Ga_{27-x}$ layers with $7 \leq x \leq 11$. The local structure was determined by means of x-ray absorption fine structure spectroscopy at Fe-K, Ga-K and Tb-L_3 edges. The increase of Tb in the alloy promotes the phase segregation that produces a larger amount of the $TbFe_2$ structural phase. The structural results have been correlated with the magnetic characterization that shows the enhancement of the out-of-plane component of the magnetization.

1. Introduction

$TbFe_2$ has been deeply studied due to its huge magnetostriction constant (λ_s) of around 4000 ppm at 10 K and 2500 ppm at room temperature [1]. Later, it was discovered the existence of perpendicular magnetic anisotropy (PMA) in this binary alloy and the influence of growth conditions and composition on it [2–7]. Nevertheless, the high coercivity and brittleness of Tb-Fe reduce the practical applications of this material. Fe-Ga alloys appeared in 2000 as an option to $TbFe_2$ due to their lower coercivity and price, combined with a higher mechanical reliability and chemical stability together with a reasonably high λ_s of 440 ppm at room temperature [8,9]. The existence of PMA in Fe-Ga has also been reported, with particular features such as rotatable magnetic anisotropy [10–12].

An interesting possibility is the combination of these two binary alloys in order to achieve a system with a lower coercivity than $TbFe_2$ but superior magnetostriction than Fe-Ga. Another option to be explored due to the existence of PMA in $TbFe_2$ and Fe-Ga for some specific conditions is tuning the out-of-plane magnetization component of thin films. Recently, there have appeared works about ternary Tb-Fe-Ga alloys in two regions of composition. On the one hand, there are reports about $Fe_{100-x}Ga_x$ alloys with x ~17 at.% and x ~27 at. % doped with a quantity of Tb not above 1 at.% [13–20]. In particular, λ_s shows an increase of ~250% in (110)-textured polycrystalline alloys doped with a 0.3 at.% of Tb [16]. The second explored compositional range has been $Tb_yFe_{100-x-y}Ga_x$ alloys with y between 7 and 11 at.% and x from 13 to 20 at.% obtained by co-sputtering [21–24], i.e. higher Tb contents than in other works. In these latter cases, studies have been focused on the PMA of the ternary alloys. One of the main differences between these two compositional regions studied so far is the microstructure. When the Tb content is rather low (below 1 at.%), it has been found by x-ray diffractometry (XRD) that typically the alloys exhibit a bcc structure similar to what is observed in Fe-Ga alloys [14] whereas it is closer to that of $TbFe_2$ in the second compositional regime for much higher Tb contents [21,22]. Nevertheless, in this Tb-rich region it has also been reported the existence of two segregated phases in co-sputtered ternary thin films $Tb_xFe_{73}Ga_{27-x}$ with 7 at. % $\leq x \leq$ 11 at. % [23]. For 7 at. % of Tb, characteristic peaks related to the presence of alloys close to both $TbFe_2$ and Fe-Ga have been observed by XRD. In general, sputtered Fe-Ga alloys with a Ga content up to 30 at. % show the same bcc

* Corresponding author.
E-mail address: rociran@ucm.es (R. Ranchal).

http://dx.doi.org/10.1016/j.jallcom.2017.07.271
0925-8388/

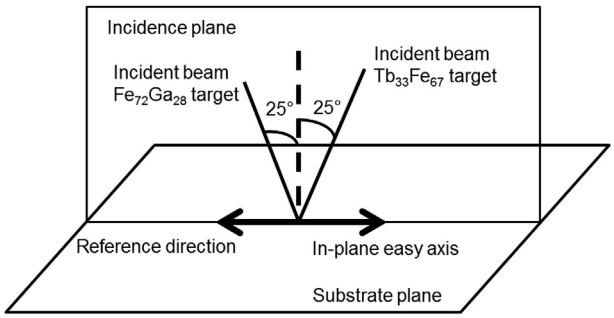

Fig. 1. Scheme of the targets configuration, sputtering beam direction and reference direction. The in-plane magnetic axis has been found to coincide with the reference direction.

Table 1
Summary of the ternary and binary alloys studied in this work.

Composition	Growth conditions
$Tb_7Fe_{73}Ga_{20}$	$TbFe_2$. DC: 50 W Fe_3Ga. DC: 90 W
$Tb_{10}Fe_{73}Ga_{17}$	$TbFe_2$. DC: 70 W Fe_3Ga. DC: 90 W
$Tb_{11}Fe_{73}Ga_{16}$	$TbFe_2$. DC: 90 W Fe_3Ga. DC: 90 W
TbFe-90	$TbFe_2$. DC: 90 W
TbFe-60	$TbFe_2$. DC: 60 W
TbFe-50	$TbFe_2$. DC: 50 W
FeGa-90	$Fe_{72}Ga_{28}$. DC: 90 W

structure as pure Fe [25,26]. The main diffraction peak that is usually observed corresponds to the (110) diffraction. This peak is shifted towards lower diffraction angles reflecting the increase of the lattice parameter because of the introduction of Ga in the bcc Fe matrix. For that reason, XRD reveals the presence of Fe-Ga alloys when the detected diffraction peaks of the Fe-bcc structure are shifted to account for this increase of lattice parameter as we have previously reported in Ref. [23]. Apart from this, it is clearly observed a diffraction peak associated with the $TbFe_2$ in that same reference. The diffraction peak related to Fe-Ga shows a decrease of its intensity as the Tb content increases along the studied range, whereas the peak related to $TbFe_2$ exhibits the opposite behavior [23]. This phenomenon is accompanied by an enhancement of the out-of-plane component of the magnetization. Nevertheless, the microstructure at the local range is not completely clear as it has been inferred from indirect measurements such as magnetization as a function of the temperature. In this work, we address the study of microstructure by x-ray absorption fine structure spectroscopy (XAFS) and its dependence with the Tb content in these Tb-Fe-Ga ternary alloys.

2. Experimental techniques

Samples were deposited at room temperature on 5 × 4 mm^2 glass substrates. Two targets with a nominal composition of $Tb_{33}Fe_{67}$ and $Fe_{72}Ga_{28}$ with a diameter of 5 cm and a thickness of 2 mm were employed to co-sputter the alloys (Fig. 1). The deposition was performed in the oblique incidence, being the angle of incidence between each target and the substrate of about 25° and the distance between targets and substrate of 9 cm, i.e. smaller than in other works [21,22,24] and the same than in Ref. [23]. Before the deposition of each sample, the base pressure was below 4×10^{-7} mbar. The Ar pressure was 2×10^{-3} mbar to evaporate all the layers: buffer, capping, ternary Tb-Fe-Ga alloys, and binary Fe-Ga and Tb-Fe films. To obtain samples with different compositions, we have fixed a DC power of 90 W in the $Fe_{72}Ga_{28}$ being modified the DC power between 50 and 90 W in the $Tb_{33}Fe_{67}$ target. In this way, we have managed to obtain the following alloys: $Tb_7Fe_{73}Ga_{20}$, $Tb_{10}Fe_{73}Ga_{17}$, and $Tb_{11}Fe_{73}Ga_{16}$. The growth rate for $Tb_7Fe_{73}Ga_{20}$ and $Tb_{10}Fe_{73}Ga_{17}$ was 0.4 nm/s, and 0.5 nm/s for $Tb_{11}Fe_{73}Ga_{16}$, respectively. The time of deposition was controlled to obtain a thickness of around 320 nm that was ex-situ measured by means of an Alphastep profiler. The XRD in the Bragg-Brentano configuration and some magnetic characterization of the ternary layers can be found elsewhere [23]. We have also grown binary Fe-Ga and Tb-Fe layers for further comparisons. Taking into account the growth conditions used for the ternary alloys, we have deposited a Fe-Ga film with a DC power of 90 W in the $Fe_{72}Ga_{28}$ target, and three

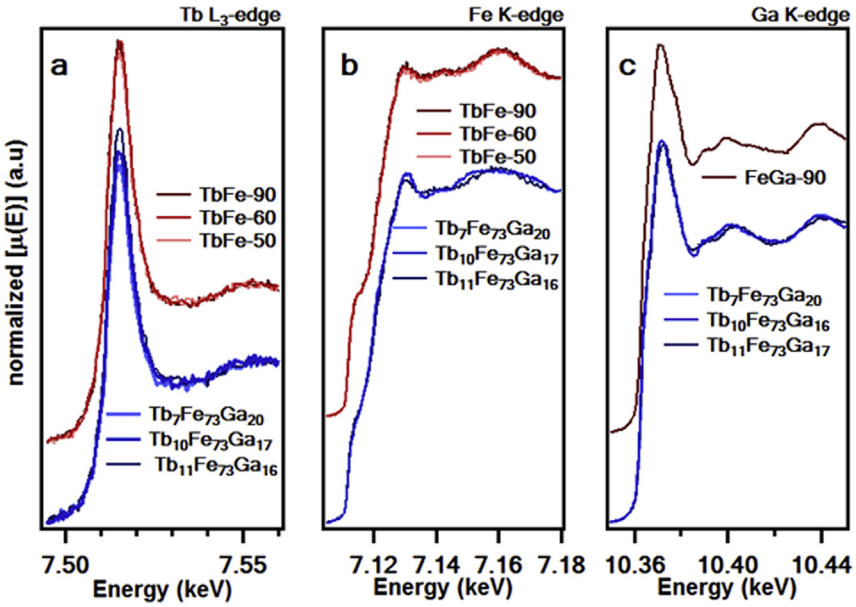

Fig. 2. Experimental XANES data for the binary and ternary alloys at the (a) Tb L_3-edge, (b) Fe K-edge, and (c) Ga-K edge.

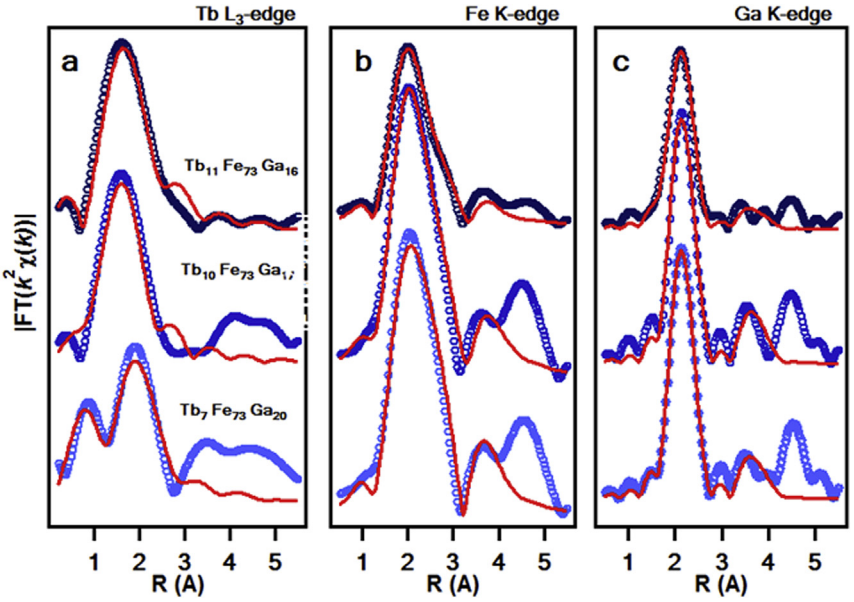

Fig. 3. Experimental EXAFS data and best fits of the ternary TbFeGa alloys at the (a) Tb L_3-edge, (b) Fe K-edge, and (c) Ga-K edge.

Tb-Fe films with a DC power of 50, 60 and 90 W in the $TbFe_2$ target. We will denote these binary films as: FeGa-90, TbFe-50, TbFe-60 and TbFe-90, respectively (Table 1). Mo 20 nm thick was used as buffer and capping layers for all the samples. They were grown with a DC power of 90 W.

Standard XAFS experiments were carried out in Tb-Fe-Ga, Fe-Ga and Tb-Fe thin films. XAFS spectra were acquired in the Tb L_3-edge, Fe and Ga K- edges in fluorescence yield mode merging from 3 to 4 single spectra. Extended x-ray absorption fine structure (EXAFS) spectra were acquired upon photoelectron wavenumber values of 15 $Å^{-1}$ for the Fe and Ga K-edges and upon 10 $Å^{-1}$ at the Tb L_3-edge. The EXAFS analysis were performed employing scattering paths calculated with FEFF8.4 code [27] using modified crystallographic structures of Fe bcc [28] to obtain the Fe-Ga and $TbFe_2$ structures [29] being both phases included to simulate the data of the ternary alloys. The Demeter software [30] was utilized for reducing the raw EXAFS data and the corresponding fits in r and k spaces. The range for the fittings were $\Delta R = 1–4$ Å and $\Delta k = 1.8–12$ $Å^{-1}$ in Fe and Ga K-edges and $\Delta R = 1–3$ Å and $\Delta k = 2–7$ $Å^{-1}$ in the Tb L_3-edge. For the fits, the number of atoms for each atomic path or coordination number has been set to the nominal value of the FEFF calculation, except for the shells including Tb. A careful energy calibration was performed, therefore the energy shift (ΔE_0), was set free for convergence reasons but never exceeded ±7 eV.

At room temperature, in-plane hysteresis loops were carried out in a vibrating sample magnetometer (VSM). In the VSM we can rotate the sample being possible to measure the in-plane loops at different angles between the applied magnetic field and the in-plane reference direction, which is taken in the sputtering beam direction (Fig. 1). We denote 0° when the applied magnetic field is applied in the reference direction.

3. Results and discussion

The XAS spectra at Tb L_3-edge for the ternary: $Tb_7Fe_{73}Ga_{20}$, $Tb_{10}Fe_{73}Ga_{17}$, and $Tb_{11}Fe_{73}Ga_{16}$, and the binary alloys: TbFe-50, TbFe-60 and TbFe-90 have been compared. X-ray absorption near edge structure (XANES) and Fourier Transform (FT) of the EXAFS spectra are included in Fig. 2 (a) and 3 (a). At first look, differences are clearer appreciated in the ternary in comparison to the binary alloys. Among the ternaries, the increase in Tb content is concomitant with the increase of the edge white line intensity. A closer look to the local range of the ternary alloys, tackled by fitting the EXAFS spectra (Fig. 3 a), allows to observe that the Tb spectra have in average a low degree of structure. There is a lack of defined features beyond the first shell, which has been firstly fitted considering a unique Tb-Tb shell. Large to very large Tb-Tb shell distance variances (σ^2) are obtained in the spectra fittings (Table 2). In the studied Tb-Fe binary alloys we fitted the spectra by considering a $TbFe_2$ structure and we observe that the coordination (N) of the Tb-Tb shell reaches the maximum at 60 W, also coinciding with the highest shell distance (R) and σ^2 (Table 2). The σ^2 values are lower in the binary respect to the ternary alloys in all cases. For the ternaries, the Tb structure in the lowest Tb content (7 at. %) layer shows two sub-shells. The distance of the first sub-shell is smaller than the corresponding to the $TbFe_2$ structure whereas the second sub-shell shows a best fit to $TbFe_2$. When increasing the Tb content a decrease in the shell variances and in the Tb-Tb shell distances can be observed (Table 2). In this case, a good agreement is achieved by considering a unique Tb-Tb shell with 7–8 coordination. All these results can be explained as follows. First of all, the first shell at about 1.6 Å can be related to the presence of Fe interstitials in the $TbFe_2$ structure of the ternary alloy with the lowest Tb content. The larger σ^2 values obtained in the ternary compared to the binary alloys indicate higher degrees of static disorder in the ternaries. In them, the progressive decrease of this parameter for increasing Tb contents points to a higher segregation of Tb to form $TbFe_2$, as already pointed out by the diffraction studies [23]. In fact, the development of a more segregated $TbFe_2$ phase should be the reason for the sharpening of the white line in the XANES upon the increase of Tb [31].

The Fe K-edge experimental data are in agreement with the Tb L_3-edge. In the XANES region of the binary Tb-Fe alloys no detectable differences have been observed amongst them (Fig. 2 b). More information has been obtained from the local structure

parameters inferred from EXAFS. The binary alloys show a considerable increase in the Fe-Tb shell distance and σ^2 upon the increase of the Tb content (Fig. 3 b and Table 2). At the Fe K-edge, in contrast to what happens at the Tb L_3-edge, the increase of σ^2 can be taken as an indication of a higher proportion of $TbFe_2$ because the enhancement of a secondary phase is expected to increase the disorder in the local environment of Fe. In the case of the ternary alloys, we observe that the raise of Tb content is also accompanied by the increase of shell variance that can be again related to the $TbFe_2$ segregation. The highest Tb content ternary alloy (11 at.%) shows the most different spectral features respect to the other layers, which is also evidenced in the distortion of the XANES spectrum respect to the 7 and 10 at.% Tb alloys (Fig. 2 b).

The data at the Ga K-edge corresponding to the ternary alloys are completely fitted by considering a Fe-Ga structural phase (Fig. 2 c) and suggest that, at least from the local point of view, there is not coexistence of Tb and Ga in a common phase (Fig. 3 c). The experimental data indicates that the Fe-Ga structure may be locally conserved for Tb contents between 7 and 10 at. % since parameters inferred from EXAFS are quite similar to the binary alloy (Table 2). However, for the highest Tb content the structure starts to become more distorted. This means that once a certain Tb in the alloy is reached (11 at. %), the formation of a rather high proportion of $TbFe_2$ in the layer affects the structural short-term order in the Fe-Ga phase, evidenced by a large increase of the shell distance variances. This last hypothesis seems to find an additional evidence in the distortion of the Ga K-edge XANES for the highest Tb content alloy.

The local structure modifications have correlation with the observed magnetic behavior of layers. All the studied ternary thin films exhibit a clear uniaxial magnetic anisotropy in the sample plane, being the direction of the easy axis coinciding with that of the sputtering beam (Fig. 1 for the scheme and Fig. 4 a, c, and e for magnetic measurements). However, the hysteresis loops in the easy axis do not exhibit a completely square shape (Fig. 4 b, d, and f) and it can be appreciated a linear behavior as the magnetization approaches the saturation being more pronounced in the layer with the highest Tb content. This linear behavior is not present in the easy axis of the binary alloy FeGa-90 (Fig. 5) and therefore, it is not related to the Fe-Ga phase existing in the ternary alloys. This linear behavior is also present in the in-plane hard axis of the ternaries alloys being promoted a widening of the low-field region of the loops (Fig. 4 b, d and f). This feature is more evident in the highest Tb content ternary film and it is not present in the FeGa-90 layer (Fig. 5). A linear behavior in the in-plane hysteresis loops is

Table 2
EXAFS parameters obtained from best fits of the experimental data: *N*, *R*, σ^2, the theoretical to experimental energy shift (ΔE_0) and the fitting correlation coefficient (r-coef).

Edge	Layer	shell	N	R (Å)	σ^2 (Å^2)	ΔE_0 (eV)	r-coef
Tb (L_3)	TbFe 50	*Tb-Tb*	5(1)	2.49(2)	0.011(1)	4(1)	0.02
	TbFe 60	*Tb-Tb*	8(1)	2.52(2)	0.020(2)	7(1)	0.02
	TbFe 90	*Tb-Tb*	7(1)	2.51(2)	0.016(1)	5(1)	0.04
	$Tb_7Fe_{73}Ga_{20}$	*Tb-Tb/Fe interstitial*	2(1)	1.63(2)	0.025(3)	2(1)	0.03
		Tb-Tb	7(1)	2.57(2)	0.030(2)	2(1)	0.03
	$Tb_{10}Fe_{73}Ga_{17}$	*Tb-Tb*	8(1)	2.49(2)	0.022(2)	4(1)	0.03
	$Tb_{11}Fe_{73}Ga_{16}$	*Tb-Tb*	7(1)	2.49(2)	0.017(2)	4(1)	0.03
Fe (K)	TbFe-50	*Fe-Fe*	8	2.44(2)	0.013(1)	−6(1)	0.01
		Fe-Tb	2(1)	2.94(2)	0.026(2)	−6(1)	0.01
		Fe-Fe	12	3.97(2)	0.028(2)	−6(1)	0.01
	TbFe-60	*Fe-Fe*	8	2.42(2)	0.016(1)	−7(1)	0.01
		Fe-Tb	12(1)	2.98(2)	0.04(1)	−7(1)	0.01
		Fe-Fe	12	3.97(2)	0.028(2)	−7(1)	0.01
	TbFe-90	*Fe-Fe*	8	2.47(2)	0.014(1)	−4(1)	0.04
		Fe-Tb	12(1)	3.02(2)	0.06(1)	−4(1)	0.04
		Fe-Fe	12	4.02(2)	0.028(2)	−4(1)	0.04
	FeGa-90	*Fe-Fe*	8	2.56(1)	0.0060(5)	−6(1)	0.03
		Fe-Ga	6	2.96(2)	0.025(3)	−6(1)	0.03
		Fe-Fe	8	4.04(2)	0.018(1)	−6(1)	0.03
	$Tb_7Fe_{73}Ga_{20}$	*Fe-Fe*	8	2.48(1)	0.0070(5)	−5(1)	0.02
		Fe-Fe	6	2.87(2)	0.014(1)	−5(1)	0.02
		Fe-Tb	3(1)	3.05(2)	0.011(1)	−5(1)	0.02
		Fe-Fe	12	4.06(2)	0.0106(5)	−5(1)	0.02
	$Tb_{10}Fe_{73}Ga_{17}$	*Fe-Fe*	8	2.49(1)	0.0069(5)	−3(1)	0.05
		Fe-Fe	6	2.88(2)	0.0087(5)	−3(1)	0.05
		Fe-Tb	1(1)	3.06(2)	0.027(2)	−3(1)	0.05
		Fe-Fe	12	4.07(2)	0.011(1)	−3(1)	0.05
	$Tb_{11}Fe_{73}Ga_{16}$	*Fe-Fe*	8	2.50(1)	0.015(1)	−4(1)	0.02
		Fe-Fe	6	2.89(2)	0.016(1)	−4(1)	0.02
		Fe-Tb	2(1)	3.07(2)	0.044(3)	−4(1)	0.02
		Fe-Fe	12	4.09(3)	0.027(2)	−4(1)	0.02
Ga (K)	FeGa-90	*Ga-Fe*	8	2.51(1)	0.0070(5)	−1(1)	0.01
		Ga-Ga	6	2.90(1)	0.022(2)	−1(1)	0.01
		Ga-Fe	9	4.10(3)	0.013(1)	−1(1)	0.01
	$Tb_7Fe_{73}Ga_{20}$	*Ga-Fe*	8	2.51(1)	0.0077(5)	1(1)	0.02
		Ga-Ga	6	2.90(1)	0.013(1)	1(1)	0.02
		Ga-Fe	9	4.10(2)	0.027(2)	1(1)	0.02
	$Tb_{10}Fe_{73}Ga_{17}$	*Ga-Fe*	8	2.51(1)	0.0078(5)	1(1)	0.02
		Ga-Ga	6	2.90(2)	0.018(1)	1(1)	0.02
		Ga-Fe	9	4.10(3)	0.010(1)	1(1)	0.02
	$Tb_{11}Fe_{73}Ga_{16}$	*Ga-Fe*	8	2.53(1)	0.012(1)	2(1)	0.01
		Ga-Ga	6	2.92(2)	0.022(2)	2(1)	0.01
		Ga-Fe	9	4.12(2)	0.022(2)	2(1)	0.01

indicative of the presence of a weak perpendicular anisotropy [10,32,33], and its enhancement reflects the increase of the out-of-plane component of the magnetization with the Tb content [23]. Considering the local range structural information, the out-of-plane component of magnetization seems to be related to the enhancement of $TbFe_2$ phase, because of the phase segregation promoted upon the increase of Tb. This would be in agreement with previous results about ternary Tb-Fe-Ga compounds in which the same explanation was concluded by means of indirect measurements [22–24].

4. Conclusions

In summary, the current results show the correlation between the Tb content and the microstructure evolution in Tb-Fe-Ga alloys. By means of an exhaustive characterization performed by XAFS we have determined how the phase segregation of $TbFe_2$ is controlled by the Tb content in the layer. Because the Tb content is determined

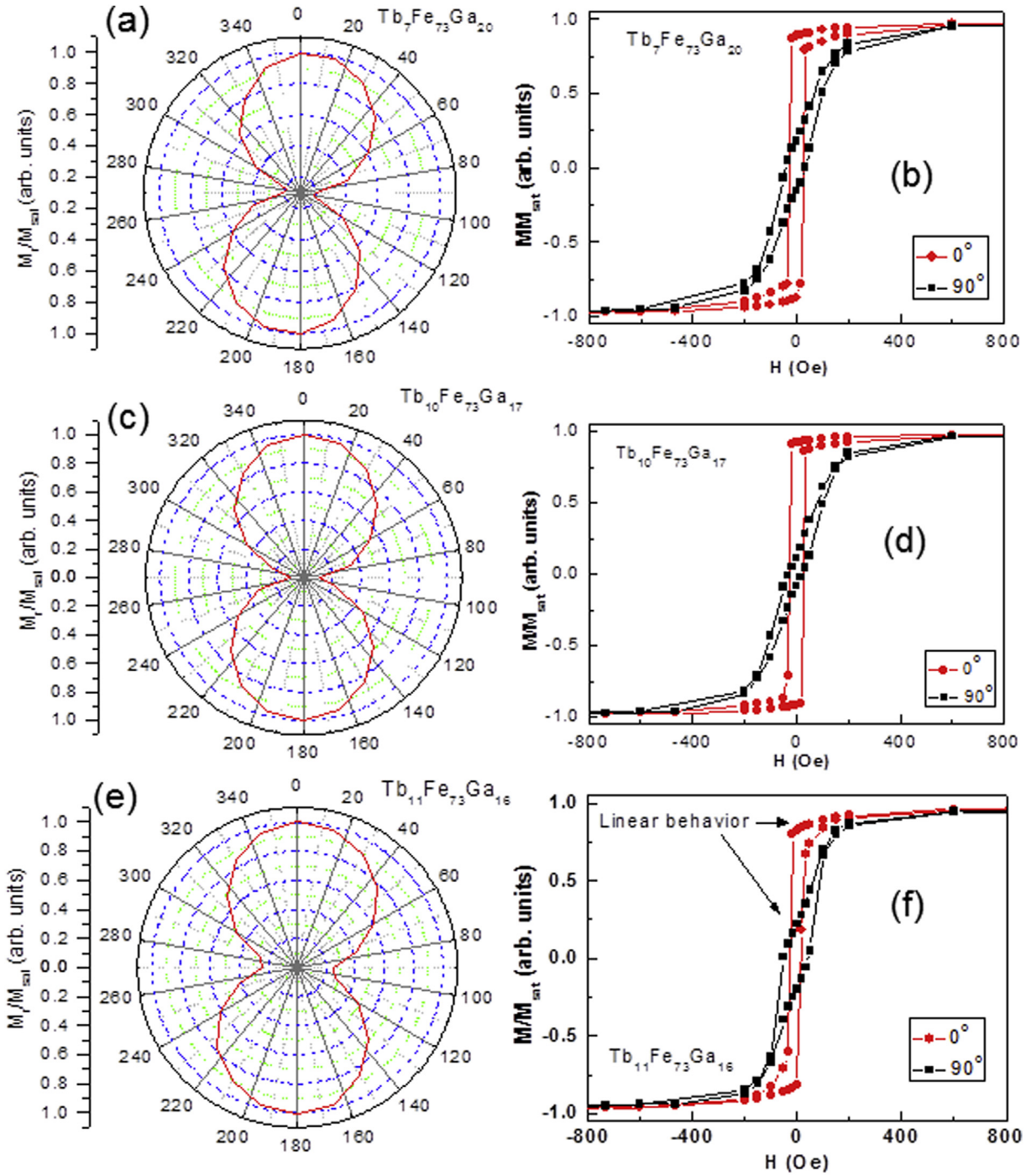

Fig. 4. Polar plot of the remanence as a function of the angle of the applied field with respect to the reference direction, i.e. the incidence sputtering beam direction that is taken as 0°. (a) $Tb_7Fe_{73}Ga_{20}$ (c) $Tb_{10}Fe_{73}Ga_{17}$, and (e) $Tb_{11}Fe_{73}Ga_{16}$. Hysteresis loops in the in-plane easy (0°) and hard directions (90°) for (b) $Tb_7Fe_{73}Ga_{20}$ (d) $Tb_{10}Fe_{73}Ga_{17}$, and (f) $Tb_{11}Fe_{73}Ga_{16}$.

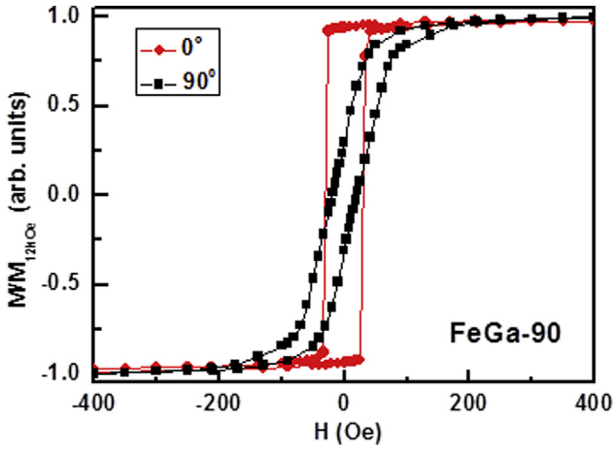

Fig. 5. Hysteresis loops in the in-plane easy (0°) and hard (90°) directions for the binary FeGa-90 film.

by the growth power, we show the possibility of tuning the layers local structure by means of the growth power in the $TbFe_2$ target. The phase segregation directly affects the in-plane magnetic behavior which also reflects the enhancement of the out-of-plane component of the magnetization.

Acknowledgements

This work has been financially supported through projects MAT2015-66888-C3-3-R and PIE-2010-OE-013-200014 of the Spanish Ministry of Economy and Competitiveness (MINECO/FEDER) and through the project PR26/16-3B-2 of Santander and Universidad Complutense de Madrid. We thank "Instituto de Sistemas Optoelectrónicos y Microtecnología" (ISOM) for using its facilities. We also want to thank ESRF and BM25-Spline, the Spanish CRG at ESRF, for providing beamtime.

References

[1] A.E. Clark, H.S. Belson, Phys. Rev. B 5 (1972) 3642.
[2] V.G. Harris, K.D. Aylesworth, B.N. Das, W.T. Elam, N.C. Koon, Phys. Rev. Lett. 69 (1992) 1939.
[3] F. Hellman, E.M. Gyorgy, Phys. Rev. Lett. 68 (1992) 1391.
[4] F. Hellman, A.L. Shapiro, E.N. Abarra, R.A. Robinson, R.P. Hjelm, P.A. Seeger, J.J. Rhyne, J.I. Suzuki, Phys. Rev. B 59 (1999) 11408.
[5] J. Huang, C. Prados, J.E. Evetts, A. Hernando, Phys. Rev. B 51 (1995) 297.
[6] V.G. Harris, T. Pokhil, Phys. Rev. Lett. 87 (2001) 067207.
[7] R. Ranchal, E. López, J.L. Prieto, C. Aroca, Acta Mater. 59 (2011) 2865.
[8] A.E. Clark, J.B. Restorff, M. Wun-Fogle, T.A. Lograsso, D.L. Schlagel, IEEE Trans. Magn. 36 (2000) 3238.
[9] Q. Xing, Y. Du, R.J. McQueeney, T.A. Lograsso, Acta Mater. 56 (2008) 4536.
[10] M. Barturen, J. Milano, M. Vásquez-Mansilla, C. Helman, M.A. Barral, A.M. Llois, M. Eddrief, M. Marangolo, Phys. Rev. B 92 (2015) 054418.
[11] S. Tacchi, S. Fin, G. Carlotti, G. Gubbiotti, M. Madami, M. Barturen, M. Marangolo, M. Eddrief, D. Bisero, A. Rettori, M.G. Pini, Phys. Rev. B 89 (2014) 024411.
[12] M. Barturen, B. Rache-Salles, P. Schio, J. Milano, A. Butera, S. Bustingorry, C. Ramos, A.J.A. de Oliveira, M. Eddrief, E. Lacaze, F. Gendron, V.H. Etgens, M. Marangolo, Appl. Phys. Lett. 101 (2012) 092404.
[13] W. Wu, J.H. Liu, C.B. Jiang, X.B. Xu, Appl. Phys. Lett. 103 (2013) 262403.
[14] T. Ma, S. Hu, G. Bai, M. Yan, Y. Lu, H. Li, X. Peng, X. Ren, Appl. Phys. Lett. 106 (2015) 112401.
[15] L. Jiang, J. Yang, H. Hao, G. Zhang, S. Wu, Y. Chen, O. Obi, T. Fitchorov, V.G. Harris, Appl. Phys. Lett. 102 (2013) 222409.
[16] T.I. Fitchorov, S. Bennet, L. Jiang, G. Zhang, Z. Zhao, Y. Chen, V.G. Harris, Acta Mater. 73 (2014) 19.
[17] I.S. Golovin, A.M. Balagurov, V.V. Palacheva, A. Emdadi, I.A. Bobrikov, A. Yu Churyumov, V.V. Cheverikin, A.V. Pozdniakov, A.V. Mikhaylovskaya, S.A. Golovi, J. Alloys Compd. 707 (2017) 51.
[18] A.M. Balagurov, I.A. Bobrikov, I.S. Golovin, V.V. Cheverikin, S.A. Golovin, Mater. Lett. 181 (2016) 67.
[19] C. Meng, H. Wang, Y. Wu, J. Liu, C. Jiang, Sci. Rep. 6 (2016) 34258.
[20] C. Meng, Y. Wu, C. Jiang, Mater. Des. 130 (2017) 183.
[21] R. Ranchal, V. Gutiérrez-Díez, Thin Solid Films 534 (2013) 557.
[22] R. Ranchal, S. Fin, D. Bisero, C. Aroca, J. Alloys Compd. 582 (2014) 839.
[23] R. Ranchal, S. Fin, D. Bisero, J. Alloys Compd. 667 (2016) 262.
[24] D. Bisero, S. Fin, R. Ranchal, Thin Solid Films 628 (2017) 158.
[25] R.A. Dunlap, N.C. Deschamps, R.E. Mar, S.P. Farrell, J. Phys. Condens. Matter 18 (2006) 4907.
[26] A. Muñoz-Noval, A. Ordóñez-Fontes, R. Ranchal, Phys. Rev. B 93 (2016) 214408.
[27] A.L. Ankudinov, B. Ravel, J.J. Rehr, S.D. Conradson, Phys. Rev. B 58 (1998) 7565.
[28] R.W.G. Wyckoff, Crystal structures, second ed., Interscience Publishers, New York, 1963.
[29] K.H.J. Buschow, R.P. van Stapele, S.D. Neov, J. Appl. Phys. 41 (1970) 4066.
[30] B. Ravel, M. Newville, J. Synchrotron Radiat. 12 (2005) 537.
[31] F. Farges, G.E. Brown Jr., J.J. Rehr, Phys. Rev. B 56 (1997) 1809.
[32] A. Hubert, R. Schäfer, Magnetic Domains, Springer, 1998.
[33] M. Romera, R. Ranchal, D. Ciudad, M. Maicas, C. Aroca, J. Appl. Phys. 110 (2011) 083910.